Bull. Chem. Soc. Ethiop. **2026**, 40(12), 2597-2607.
DOI: https://dx.doi.org/10.4314/bcse.v40i12.7

ISSN 1011-3924
Printed in Ethiopia
Online ISSN 1726-801X
© 2026 Chemical Society of Ethiopia and The Authors

SHORT COMMUNICATION

STUDY ON THE PREPARATION OF IRON SULFIDE MATERIALS USING PRECIPITATION AND THEIR ELECTROCHEMICAL PERFORMANCE IN SODIUM-ION BATTERIES

Zhanqing Lv[1], Shilei Cao[3], Binning Lu[1], Dunqing Wang[1], Min Yang[1], Wenwen Liu[1,2], Man Qi[1,2], Wenyu Wu[1,2], Qingchao Zhang[4], Jianzhi Sun[1,2*], Manman Ren[3*]

[1]College of Chemistry and Chemical Engineering, Dezhou University, Shandong Dezhou, 253023, P.R. China
[2]Shandong Provincial Key Laboratory of Monocrystalline Silicon Semiconductor Materials and Technology, Dezhou University, Dezhou 253023, China
[3]School of Materials Science and Engineering, Qilu University of Technology (Shandong Academy of Sciences), Jinan 250353, P.R. China
[4]Dezhou Taiding New Material Technology Ltd., Dezhou 253100, P.R. China

(Received February 23, 2026; Revised August 7, 2026; Accepted September 3, 2026)

ABSTRACT. Sodium-ion batteries are undergoing a pivotal transition from pilot-scale demonstrations to large-scale commercialization. As an anode material, FeS_2 demonstrates outstanding potential for industrial application owing to its high theoretical specific capacity, abundant crustal reserves, low raw material cost, environmental compatibility, and excellent electrochemical reversibility. In this work, we report a green, controllable, and industrially viable synthesis of FeS_2 achieved under ambient pressure and room-temperature conditions, integrating liquid-phase precipitation with subsequent calcination and sulfidation. Critically, all process steps are compatible with continuous-flow manufacturing, enhancing translational feasibility. The resulting material was systematically characterized in terms of its microstructure, crystallographic features, and electrochemical energy storage behavior. Electrochemical tests revealed a high initial discharge capacity of 430 mAh g^{-1} at a high current density of 2 A g^{-1}, with the reversible capacity remaining above 325 mAh g^{-1} after 130 cycles, demonstrating excellent rate capability and long-term cycling stability. This work establishes a scalable, experimentally validated route to high-performance, cost-effective FeS_2 anodes directly addressing key material-level bottlenecks hindering the industrial deployment of sodium-ion batteries.

KEY WORDS: Sodium-ion battery, Liquid-phase precipitation method, FeS_2, Anode material

INTRODUCTION

Energy serves as the cornerstone of modern society. However, the rapid depletion of fossil fuel reserves and the escalating environmental challenges associated with their combustion have intensified global efforts to advance the generation, storage, and utilization of clean, renewable energy sources [1, 2]. In alignment with this imperative, China has formally committed to achieving carbon peak by 2030 and carbon neutrality by 2060. Realizing these targets necessitates not only the large-scale deployment of green and sustainable energy generation technologies but also the concurrent development of safe, efficient, and scalable energy storage systems. Among emerging storage solutions, electrochemical energy storage particularly due to its cost-

*Corresponding authors. E-mail: jianzhisun@163.com
This work is licensed under the Creative Commons Attribution 4.0 International License

effectiveness, high round-trip efficiency, and modular scalability holds significant promise for supporting grid stability and enabling deep decarbonization [3-5].

Rechargeable lithium-ion batteries (LIBs) currently dominate the markets for portable electronics and electric vehicles, owing to their high energy and power densities, technological maturity, and well-established manufacturing infrastructure. Nevertheless, their widespread adoption faces critical constraints including limited global lithium reserves, geopolitical concentration of raw material supply, rising material costs, and safety concerns highlighting the strategic importance of developing next-generation alternatives. Sodium-ion batteries (SIBs) have emerged as a compelling complement to LIBs, drawing substantial research interest due to their abundant sodium resources, low raw material cost, intrinsic thermal and chemical stability, superior low-temperature performance, rapid charge/discharge capability, environmental benignity, and straightforward recyclability [6-12].

Importantly, SIB development is not intended to supplant LIBs outright, but rather to address specific application niches where their inherent advantages align closely with system-level requirements: namely, light-duty commercial vehicles, urban logistics trucks, and stationary energy storage systems. These use cases prioritize cost sensitivity, operational safety, and low-temperature reliability over volumetric or gravimetric energy density—characteristics that render SIBs particularly well-suited. Geologically, sodium is highly abundant (crustal abundance: ~2.75%), widely distributed, and inexpensive (~CNY 2/kg), whereas lithium is scarce (crustal abundance: ~0.0065%), geographically concentrated (primarily in South America and Australia), and costly (~CNY 150/kg). Moreover, SIBs employ aluminum foil for both cathode and anode current collectors eliminating the need for expensive copper foil used in LIBs—and thereby reduce material costs by 30-40% [13, 14].

At present, in sodium-ion batteries (SIBs), anode materials are primarily categorized into four types based on their electrochemical reaction mechanisms: intercalation-type (e.g., hard carbon and graphene), alloying-type, conversion-type, and organic anode materials. Among these, transition metal sulfides have emerged as a particularly promising class due to their distinctive physicochemical properties, attracting increasing attention as a key research direction. These materials generally exhibit high theoretical sodium-storage capacities, stemming from their ability to undergo multi-electron redox reactions. Moreover, compared with their oxide counterparts, sulfides typically demonstrate superior electronic conductivity and faster ionic diffusion kinetics advantages that significantly enhance the rate capability and cycling stability of SIBs. In addition, transition metal sulfides display excellent redox reversibility during charge/discharge processes, which contributes to structural integrity and extended battery lifespan.

Among various transition metal compounds, iron disulfide (FeS_2) stands out as a highly compelling candidate [15-17]. FeS_2 is abundant in natural resources, low-cost, and free of toxic elements, rendering it an environmentally benign semiconductor material. Its crystal structure belongs to the cubic system, where Fe^{2+} ions are covalently bonded to $[S_2]^{2-}$ dimers endowing the material with relatively high electronic conductivity and unique electrochemical activity. Owing to these favorable attributes, FeS_2 has garnered sustained interest from both academia and industry as a next-generation anode material with exceptional application potential for SIBs. To date, common synthetic approaches for FeS_2 include solvothermal synthesis, hydrothermal synthesis, and the collaborative etching precipitation (CEP) method. Nevertheless, each of these methods faces substantial challenges when transitioning from laboratory-scale development to practical implementation and industrial production. First, the solvothermal method typically requires sealed, high-pressure autoclaves and employs high-boiling-point organic solvents such as ethylenediamine, benzyl alcohol, or oleylamine as reaction media [18, 19].

These solvents are not only expensive and highly toxic but also prone to volatilization or thermal decomposition at elevated temperatures, posing potential risks to operator health and ecological safety. Furthermore, solvent recovery and waste treatment entail considerable cost and complexity, conflicting with the principles of green chemistry and sustainable development.

Second, although the hydrothermal method uses water as the solvent a more environmentally benign choice it commonly demands prolonged reaction times (typically 12-48 h) under high temperature (150-200 °C) and corresponding saturated vapor pressure. This leads to high energy consumption, extended processing cycles, and poor controllability over product morphology and crystalline phase, resulting in limited batch-to-batch reproducibility. The CEP method, which leverages synergistic acid–base interactions to achieve controlled dissolution and reprecipitation of metal precursors, offers partial tunability of FeS_2's microstructure. However, its multistep protocol with stringent pH regulation requirements imposes high demands on equipment sophistication and operational precision.

More critically, all aforementioned methods rely heavily on high-temperature and/or high-pressure conditions, imposing rigorous requirements on autoclave material quality, sealing performance, and operational safety. Consequently, capital investment and maintenance costs are substantial, hindering scalability toward continuous, automated, large-scale industrial manufacturing.

In summary, while existing synthetic strategies enable successful laboratory-scale preparation of FeS_2, they remain hampered by significant bottlenecks concerning cost efficiency, environmental compatibility, process simplicity, and scalability. Therefore, the development of a green, scalable synthesis route operating under low-energy input, using non-toxic solvents, and compatible with ambient or near-ambient pressure and temperature conditions is now a critical and urgent priority for advancing FeS_2-based anode materials toward commercialization in sodium-ion battery technology.

This study reports the synthesis of an iron sulfide precursor via a room-temperature liquid-phase precipitation method, followed by solid-state sulfidation. Subsequently, the resulting material was fabricated into electrodes and assembled into sodium-ion batteries. The electrochemical performance of the batteries was systematically evaluated using galvanostatic charge/discharge cycling, cyclic voltammetry, and electrochemical impedance spectroscopy. The room-temperature liquid-phase precipitation method described herein offers several advantages including low energy consumption, high atomic utilization efficiency, scalability for industrial production, absence of hazardous by-products, and environmental benignity thereby providing a promising new strategy for the large-scale fabrication of cathode materials for sodium-ion batteries.

EXPERIMENTAL

Sample preparation

The preparation of the precursor was initiated by dissolving 1.6 g $FeCl_3$ in 20 mL of deionized water, followed by the sequential addition of 5.5 mL of ammonium polysulfide solution with continuous stirring for 3 h to form a homogeneous solution. The precipitate was collected through centrifugation and subsequently washed with deionized water and ethanol (3 cycles each). The purified product was finally dried in a vacuum oven at 60 °C for 12 h.

The preparation of FeS_2 involved homogeneously blending the as-prepared precursor with sulfur powder at a mass ratio of 2:3 using an agate mortar. The mixture was then transferred to a ceramic vessel, heated at 550 °C in a tubular furnace under Ar for 4 h, and then cooled naturally to room temperature. This process yielded the black FeS_2 powder.

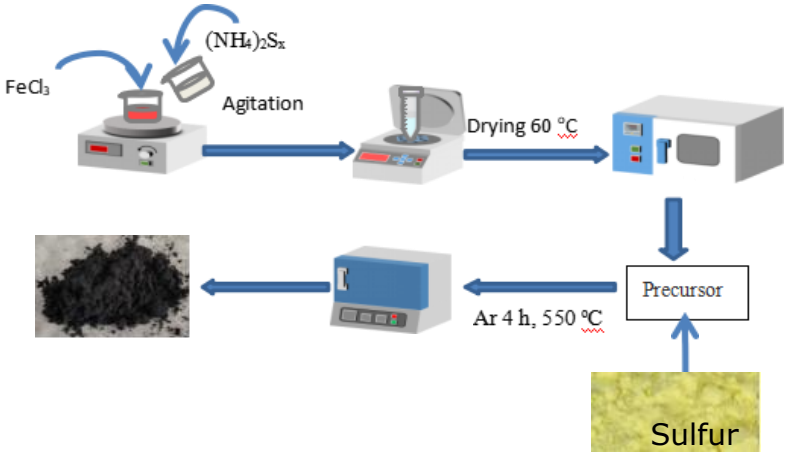

Figure 1. Preparation flow chart of the FeS_2 materials.

Characterization of materials

X-ray diffraction (XRD) was performed on a Bruker D8A25 X-Ray diffractometer, the X-ray beam was nickel-filtered Cu K (λ=0.15406 nm) radiation operated at 40 kV and 30 mA; and the data were collected from 10 ° to 80 °(2θ) at a scanning rate of 5 °/min. Thermal analysis (TG) was carried out on a NETZSCH STA 449 F5 equipment, operated under Air atmosphere. The samples were heated from room temperature up to 450 °C at heating rates of 10 °C/min. The morphology of the samples was observed by JEOL JSM-5600LV SEM. EDX analysis was observed by Oxford Instruments.

Electrochemical measurements

The electrode slurry was formulated by homogeneously dispersing active materials (FeS_2), acetylene black, and polyvinylidene fluoride (PVDF) in N-methyl-2-pyrrolidone (NMP) solvent at a mass ratio of 7:2:1. Planetary ball milling was conducted for 4 h at 400 rpm to ensure the uniform dispersion of electrode slurry. The resulting slurry was doctor-blade coated onto copper foil and then dried in a vacuum oven at 60 °C for 12 h.

For electrochemical evaluation, CR2032-type coin cells were assembled in an argon-filled glovebox, metal sodium was used as the reference electrode and counter electrodes, and glass fiber (GF, Whatman) was utilized as the separator. The electrolyte was 1.0 mol L^{-1} $NaSO_3CF_3$ dissolved in the diglyme. Galvanostatic charge-discharge (GCD) profiles were recorded on NEWARE battery test systems (BTS) under varying current densities (0.1-5 A g^{-1}) within a voltage window of 0.3-3.0 V (vs. Na^+/Na). Cyclic voltammetry measurements were performed using an electrochemical workstation (CHI760E) at different scan rates. Electrochemical impedance spectroscopy (EIS) analysis was conducted in the frequency domain of 100 kHz to 10 mHz with an AC amplitude of 5 mV. The Galvanostatic Intermittent Titration Technique (GITT) were also conducted on NEWARE BTS, with a potential range of 0.3~3.0 V (vs. Na^+/Na). In the GITT test, the voltage range is 0.3~3 V, the current density is 0.2 A g^{-1}, and the interval between two titrations is 5 min^1.

RESULTS AND DISCUSSION

XRD studies

Figure 2 presents the XRD pattern of the synthesized FeS_2 sample. The sharp and well-defined diffraction peaks indicate the sample possesses high crystallinity. The diffraction peaks are observed at 2θ values of 28.4574°, 33.0504°, 37.0283°, 40.8217°, 47.4037°, 56.3233°, 59.0709°, 61.6545°, 64.3406° and 78.8579°, which are basically consistent with those of the standard PDF card for pyrite-type FeS_2 (JCPDS No. 42-1340). The corresponding Miller indices of the crystal planes are (111), (200), (210), (211), (220), (311), (222), (023), (321) and (420), confirming that the synthesized product is pyrite-type FeS_2, which belongs to the cubic crystal system with a Pa-3 space group and a lattice constant of a = b = c = 0.54179 nm[20].

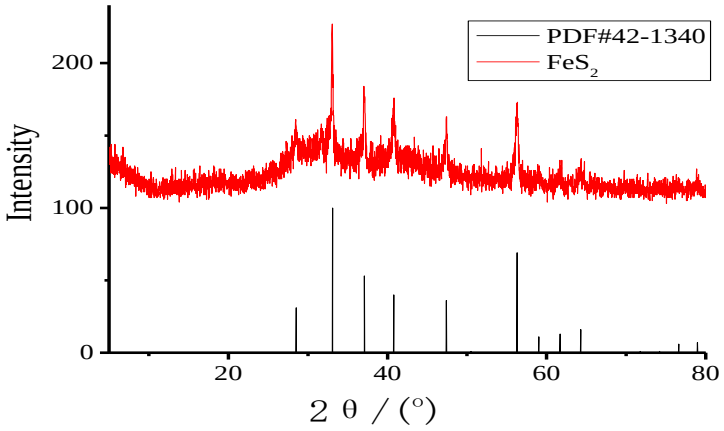

Figure 2. The XRD patterns of FeS_2 sample.

Table 1. Comparison of XRD values between the sample and the standard pattern (JCPDS 42-1340).

Crystal plane (h k l)	Sample	Reference values
1 1 1	28.4574	28.512
2 0 0	33.0504	33.083
2 1 0	37.0283	37.106
2 1 1	40.8217	40.783
2 2 0	47.4037	47.410
3 1 1	56.3233	56.278
0 2 3	61.6545	61.692
3 2 1	64.3406	64.281

SEM analysis

The morphology of the material was characterized using field-emission scanning electron microscopy (FE-SEM). As shown in Figure 3, the prepared FeS_2 sample predominantly exhibits a uniform spherical morphology, with an average particle size ranging from 50 to 100 nm. The SEM images clearly reveal that these microspheres possess smooth and intact surfaces, indicating good crystallinity. Notably, although the spheres exhibit a smooth morphology, they are not closely packed; instead, they form a unique secondary structure through partial interconnection.

This specific arrangement preserves abundant voids between the spherical particles. These three-dimensional interconnected channels not only effectively increase the specific surface area of the material but also provide sufficient buffer space for electrolyte infiltration and rapid ion transport, thereby helping to accommodate volume expansion during the charge/discharge processes. Consequently, this structure enhances the utilization of the active material and promotes the full realization of its electrochemical performance [21, 22].

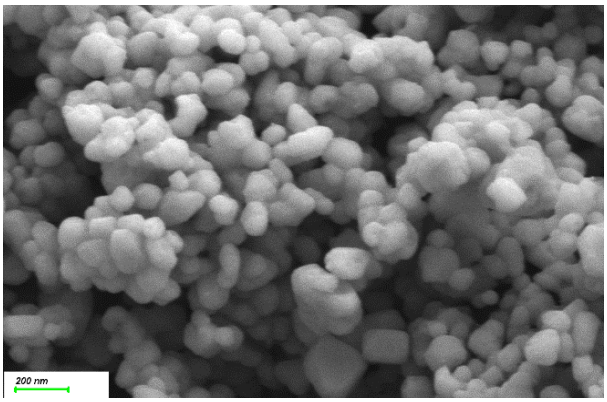

Figure 3. SEM images of FeS_2 sample (200 nm).

EDS analysis

Figures 4 show the EDS spectra of FeS_2. As can be seen from these figures, the molar ratio of Fe to S in the material is approximately 1:1.98, which is consistent with the theoretical value. All elements (Fe and S) in FeS_2 display a highly uniform spatial distribution within the particles, and no obvious elemental segregation or phase separation is detected. This indicates that FeS_2 has excellent chemical homogeneity and structural consistency at the microscale, confirming that the crystal growth is uniform during the preparation process. This provides a crucial structural foundation for improving the electrochemical performance of the electrode material [23].

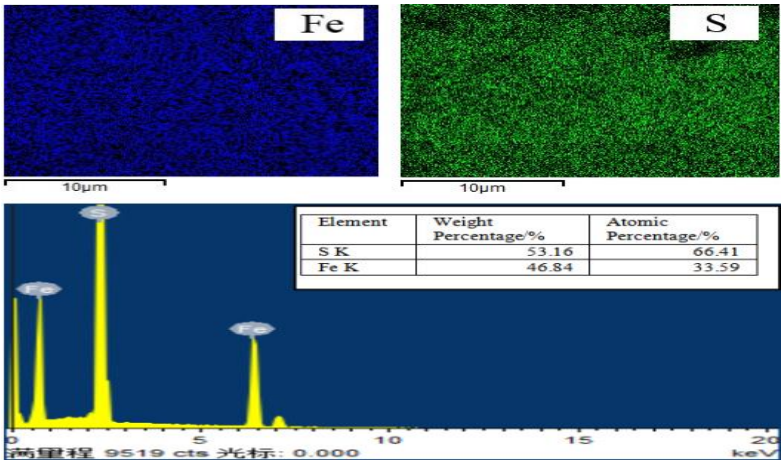

Figure 4. EDS spectra of FeS_2 sample.

Electrochemical performance

FeS_2 exhibits excellent electrochemical activity (Figure 5): the first discharge specific capacity is as high as 430 mAh g^{-1}, with a wide discharge plateau and a low potential (~1.2 V), indicating that it has abundant electrochemically active sites and good reaction kinetics; after three cycles of activation, the reversible specific capacity remains stable above 360 mAh g^{-1}, highlighting its high intrinsic sodium storage capacity and structural durability.

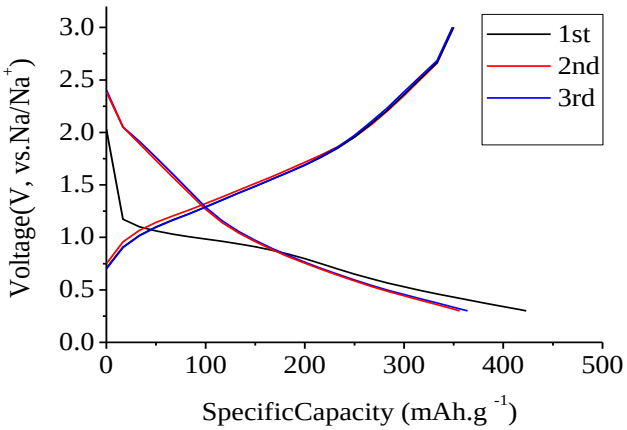

Figure 5. Constant current charging and discharging curves of FeS_2 at 2A g^{-1}.

As shown in Figure 6, At 1 A g^{-1}, FeS_2 delivers an initial discharge capacity of 482 mAh g^{-1}. After 130 cycles, it retains 325 mAh g^{-1} (67.4% retention), while Coulombic efficiency rises rapidly to > 99% by the second cycle and remains exceptionally stable fluctuating by < 0.2% throughout cycling. This sustained high reversibility, combined with negligible capacity fade and absence of voltage decay or hysteresis growth, strongly excludes dominant degradation pathways including metallic Na dendrite growth, particle isolation due to pulverization, or progressive electrolyte decomposition thereby affirming it's structural integrity and electrochemical reliability for practical medium-to-long-duration energy storage applications.

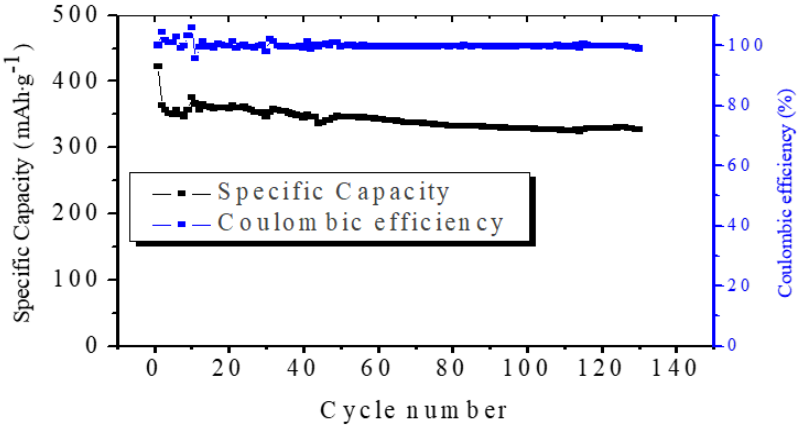

Figure 6. Cycling performance of FeS_2 electrode at 2 A g^{-1}.

Cyclic voltammogram

The CV curves of FeS_2 at different scan rates (0.2–1.0 mV s^{-1}) (Figure 7) show that the characteristic reduction peak (~1.2 V) and oxidation peak (~2.0 V) remain sharp, stable in position, and without significant broadening or intensity attenuation as the scan rate increases, confirming that the electrode maintains rapid interfacial charge transfer and excellent kinetic response even at high rates.

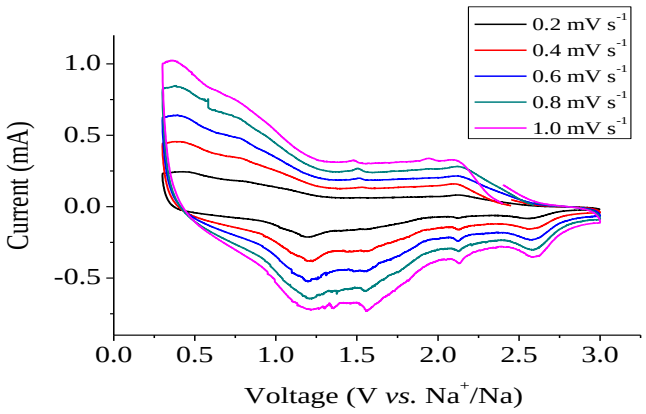

Figure 7. CV profiles at various scan rates of FeS_2.

Two-cycle CV tests (Figure 8) conducted at a scan rate of 0.2 mV s^{-1} and a voltage window of 0.3–3.0 V (vs Na^+/Na) further reveal the reaction mechanism: in the first cycle's cathodic scan, the reduction peak at 1.0 V corresponds to the reversible intercalation of Na^+ into the FeS_2 lattice to form the Na_xFeS_2 phase; the strong reduction peak at 0.2 V is attributed to the in-situ formation of the SEI film and the irreversible transformation reaction of FeS_2, The chemical equation for the reaction is shown below:

$$FeS_2 + 4Na^+ + 4e^- \rightarrow Fe + 2Na_2S$$

In the anodic scan, the oxidation peaks at 1.1 V, 1.4 V, and 2.2 V are respectively attributed to the cooperative re-oxidation of Na_2S and Fe, as well as the reversible formation of the Na_xFeS_2 phase. Notably, the intercalation peak at 1.0 V completely disappears in the second cycle's CV, confirming the essential irreversibility of this intercalation process; in subsequent cycles, the positions of the transformation-type redox peaks remain stable, the peak shapes are highly consistent, and there is no significant polarization, indicating that a stable reaction interface and reversible transformation mechanism have been established after the first cycle's activation, providing a solid electrochemical foundation for the electrode's long-term cycling stability and high Coulombic efficiency.

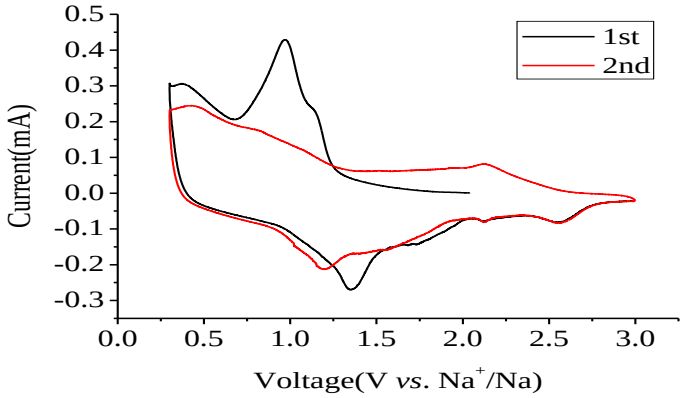

Figure 8. CV curves of the first and second cycles at the rate of 0.2 $mV.s^{-1}$.

Electrochemical impedance spectroscopy

The Nyquist plot (Figure 9) exhibits a compact high-frequency semicircle with a diameter of ~10 Ω—corresponding to an exceptionally low charge-transfer resistance (R_{at}), attributable to enhanced electronic conductivity and improved electrode/electrolyte interfacial contact. In the low-frequency region, the linear Warburg tail displays a slope of ~1.0 in the Z' vs $\omega^{-0.5}$ plot, confirming near-ideal semi-infinite diffusion of Na^+ ions within the electrode bulk, with high diffusivity and minimal concentration polarization. Together, these features establish FeS_2 as a kinetically superior electrode, integrating rapid interfacial electron transfer with efficient bulk-ion transport—key prerequisites for high-power sodium-ion battery operation.

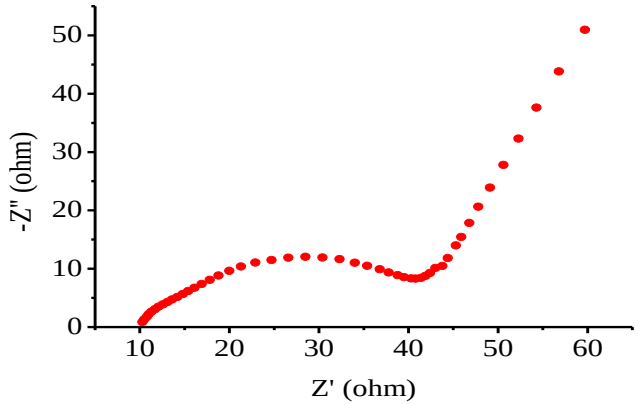

Figure 9. Nyquist plots of FeS_2 electrodes.

CONCLUSION

In summary, this work reports a green, scalable synthesis strategy for FeS_2 anode material in sodium-ion batteries, based on ambient-temperature and ambient-pressure liquid-phase precipitation, followed by calcination and sulfidation. The process is operationally simple, energetically mild, and avoids both extreme conditions (e.g., high temperature/pressure) and

hazardous organic solvents—thereby offering strong potential for continuous, industrially viable production. Electrochemical characterization reveals that the as-synthesized FeS_2 delivers a broad, stable discharge plateau near 1.2 V vs. Na^+/Na, reflecting abundant electrochemically active sites and favorable reaction kinetics. At a high current density of 1 A g^{-1}, it maintains a reversible specific capacity exceeding 325 mAh g^{-1} over extended cycling. Furthermore, Coulombic efficiency rises rapidly and stabilizes above 99% from the second cycle onward, with minimal fluctuation even after prolonged cycling demonstrating exceptional intrinsic sodium-storage capability and structural integrity. Collectively, these results underscore the promise of this FeS_2 anode for medium- to long-duration energy storage applications demanding high electrochemical stability and reliability. Beyond establishing liquid-phase precipitation as a viable route for FeS_2 synthesis, this study provides a generalizable, sustainable framework for the scalable manufacturing of other high-performance transition metal sulfides.

ACKNOWLEDGEMENTS

The authors acknowledge financial assistance from the Undergraduate University Teaching Reform Research Project of Shandong (Z2023188), Shandong Province Natural Science Foundation (ZR2023QB294, ZR2025QC1806Z) and Shandong Provincial Key Laboratory of Monocrystalline Silicon Semiconductor Materials and Technology (2025KFKT015).

REFERENCES

1. Kim, H; Hong, J; Park, K.Y.; Kim, H; Kim, S.W.; Kang, K. Aqueous rechargeable Li and Na ion batteries. *Chem. Rev.* **2014**, 114, 11788-11827.
2. Zeng, Z.Q.; Murugesan, V.; Han, K.S.; Jiang, X.Y.; Cao, Y.L.; Xiao, L.F.; Ai, X.P.; Yang, H.X.; Zhang J.G.; Sushko M.L.; Liu J. Nonflammable electrolytes with high salt-to-solvent ratios for Li-ion and Li-metal batteries. *Nature Energy* **2018**, 3, 674-681.
3. Khaoula, M.; Sihem, O.; Samia, A.; Sameh, A.; Jalgham, R.T.T.; Rabeh, R. Synthesis and characterization of graphene oxide-zinc oxide nanocomposite thin films: Enhanced photocatalytic and electrochemical properties. *Bull. Chem. Soc. Ethiop.* **2025**, 39, 1893-1907.
4. Ergete, A.; Huang, Y.F.; Zhou, J.W.; Getachew, T.; Taye, A.; Xia, R.D.; Iwuoha, E.I.; Peng, X.W.; Admassie, S. N-Doped activated carbon derived from water hyacinth for ultra-stable metal-free bifunctional electrode for zinc-air battery. *Bull. Chem. Soc. Ethiop.* **2024**, 38, 571-584.
5. Sun, J.Z.; Dong, Y.; Wang, X.F.; Cao, J.T.; Gong, M.; Li, C.H. Microrods of MoO_3 synthesized using corn straw as a biological template and their electrochemical performance in an aqueous aluminum-ion. *Bull. Chem. Soc. Ethiop.* **2021,** 35, 669-675.
6. Gong, S.G.; Shi, Y.H.; Su, Y.; Li, Y.F.; Ding, L.; Lin, J.; Yang, G.D.; Li, B.; Wu, X.L.; Zhang, J.P.; Xie, H.M.; Sun, H.Z. In situ growth of 3D Lamellar $Mn(OH)_2$ on CuO-coated carbon cloth for flexible asymmetric supercapacitors with a high working voltage of 2.4 V. *ACS Sustainable Chem. Eng.* **2021**, 9, 39, 13385-13394.
7. Zhao, J.; Ji, G.C.; Zhang, X.L.; Hu, R.F.; Zheng, J.P. Preparation of a high strength, rapid self-healing composite gel and its application in electrochemical capacitor. *Polymer*. **2021**, 214, 123372.
8. Lin, H.; Zhang, Y.X.; Huang, Y. Unlocking the intercalation mechanism of blue phosphorene/MBene heterostructures for lithium/sodium-ion batteries: A first principles study. *J. Molecular Liquids,* **2024,** 409, 125528.
9. Xiao, Z.Y.; Zhu, X.B.; Wang, S.G.; Shi, Y.H.; Zhang, H.M.; Xu, B.B.; Zhao, C.F.; Zhao, Y. Construction of uniform LiF coating layers for stable high-voltage $LiCoO_2$ cathodes in lithium-ion batteries. *Molecules* **2024,** 29, 1414.

10. Zhao, C.F.; Liu, H.Y.; Liu, J.W.; Shi, Y.H.; Wang, S,G.; Tang, Q.W.; Zhu, X.B.; Zhang, H.M.; Zhao, Y. Petal-like Mn-doped α-$Ni(OH)_2$ nanosheets for high-performance Li-S cathode material. *RSC Adv.* **2023**, 13, 8706-8717.
11. Qiu, S.; Yan, W.N.; Wang, L.; Zhang, L.S.; Chen, C.; Mu, L.J.; Mu, S.G. Facile synthesis of Si@$LiAlO_2$ nanocomposites as anode for lithium-ion battery. *Chin. J. Inorg. Chem.* **2022**, 38, 1655-1662.
12. Sun, Y.; Li, C.F.; Gao, H.C.; Li, J.M.; Hao, J.B. Liquid-combustion synthesis of spinel $LiMn_2O_4$ cathode material for enhanced electrochemical performance lithium-ion batteries. *Bull. Chem. Soc. Ethiop.* **2024**, 38, 1429-1437.
13. Ma, X.X.; Zhang, H.; Liu, Y.; Yan, W.N.; Chen, C.; Zhang, K. MOF-derived $Na_3V_2(PO_4)_3$-carbon@graphene fibers for flexible fiber-shaped sodium ion battery. *J. Electroanal. Chem.* **2024**, 975, 118740.
14. Meng, Y.; Yi, F.J.; Yang, M.Z.; Zhang, J.H.; Lv, Z.Q.; Liu, W.L.; Yao, J.S.; Sun, J.Z.; Ren, M.M. Hydrangea-shaped $FeCoS_2$@C hollow nanospheres as a dual-functional mediator for efficient polysulfide adsorption and catalysis. *J. Power Sources* **2026**, 678, 240116.
15. Liu, M.L.; Sun, J.Z.; Guo, H.L.; Yang, M.Z.; Zhang, J.H.; Liu, W.L.; Yao, J.S.; Ren, M.M. Rational design of a $Fe_{1-x}S/FeS_2$ homologous heterostructure with exceptional high-rate performance for advanced sodium-ion battery anodes. *J. Mater. Chem. A* **2025**, 13, 38504-38510
16. Zhang, K.; Zhang, H.; Li, C.X.; Ma, X.X. Vertically oriented $MoSe_{0.4}S_{1.6}$/N-doped C nanostructures directly grown on carbon nanotubes as high-performance anode for potassium-ion batteries. *J. Electroanal. Chem.* **2022**, 904, 116846.
17. Sun, J.Z.; Wang, X.F.; Wang, D.Q.; Yang, M. An enzyme-free electrochemical glucose sensor based on ordered porous Co_3O_4 material. *Bull. Chem. Soc. Ethiop.* **2025**, 39, 807-815.
18. Qin, S.Y.; Huang, L.; Shu, X.; Yang, J.; Cheng, S.Q.; Wang, Y.L. FeS_2 nanosheets as mimetic peroxidase for sensitive colorimetric detection of biothiols. *Bull. Chem. Soc. Ethiop.* **2025**, 39, 1699-1711.
19. Feng, D.; Tang, S.; Xu, H.; Zeng, T. High performance sodiumion anodes based on $FeSb_2S_4$/Sb embedded within porous reduced graphene oxide/carbon nanotubes matrix. *J. Alloys Compd.* **2023**, 931, 167576.
20. Sandhya, V.; Goban, K.P.; Pratap, K.; Kwan, J.S.; Nirmala, G.A. Solvothermal synthesis and electrochemical properties of phase pure pyrite FeS_2 for supercapacitor applications. *Electrochim. Acta* **2018**, 290, 378-389.
21. Zheng, X.Y.; Luo, J.Y.; Lv, W.; Wang, D.W.; Yang, Q.H. Two-dimensional porous carbon:synthesis and ion-transport properties. *Adv. Mater.* **2015**, 27, 5388-5395.
22. Wu, Z.S.; Sun, Y.; Tan, Y.Z.; Yang, S.; Feng, X.; Mullen, K. Three-dimensional graphene-based macro-and mesoporous frameworks for high-performance electrochemical capacitive energy storage. *J. Am. Chem. Soc*. **2012**, 134, 19532-19535.
23. Liu, N.; Wang, X.; Liu, J.; Liu, N.; Wang, L. Synergistic intercalation-conversion reaction mechanism in Prussian blue analogue materials toward enhanced Na-storage. *Chem. Sci.* **2025**, 16, 14724-14732.